MATERIALS SCIENCE

Visualization of nonsingular defect enabling rapid control of structural color

Han Sol Kang[1]†, Chanho Park[1]†, Hongkyu Eoh[1,2], Chang Eun Lee[1], Du Yeol Ryu[3], Youngjong Kang[4], Xuenyan Feng[2], June Huh[5,6]*, Edwin L. Thomas[2]*, Cheolmin Park[1,7]*

Stimuli-interactive structural color (SC) of a block copolymer (BCP) photonic crystal (PC) uses reversible alteration of the PC using external fluids and applied forces. The origin of the diffusional pathways of a stimulating fluid into a BCP PC has not been examined. Here, we directly visualize the vertically oriented screw dislocations in a one-dimensional lamellar BCP PC that facilitate the rapid response of visible SC. To reveal the diffusional pathway of the solvent via the dislocations, BCP lamellae are swollen with an interpenetrated hydrogel network, allowing fixation of the swollen state and subsequent microscopic examination. The visualized defects are low-energy helicoidal screw dislocations having unique, nonsingular cores. Location and areal density of these dislocations are determined by periodic concentric topographic nanopatterns of the upper surface-reconstructed layer. The nonsingular nature of the interlayer connectivity in the core region demonstrates the beneficial nature of these defects on sensing dynamics.

INTRODUCTION

Structural colors (SCs) in the visible regime arise from the reflection of light with wavelengths corresponding to the photonic bandgaps of periodic dielectric materials [photonic crystals (PCs)] consisting of a repeating arrangement of two components having differing refractive indices (*1*–*4*). The SCs afford great potential for emerging stimuli-interactive applications such as human interactive displays, sensors, and pattern encryptions (*5*–*7*). PCs based on self-assembled block copolymers (BCPs) (*5*) are advantageous as their periodicities and dielectric constants can be readily altered by many diverse forces such as electric (*8*–*12*), magnetic (*13*, *14*), thermal (*7*, *15*, *16*), solvating (*17*, *18*), and mechanical (*19*–*22*). This reversible alteration of the SC upon external stimulation makes these PCs suitable for human-interactive electronics where, for example, the change of body skin strain, temperature, and finger humidity can be dynamically visualized via changes in the SC of a BCP PC (*6*, *15*, *19*, *23*). For these purposes, a BCP PC frequently requires a swelling agent to sufficiently enlarge the pristine self-assembled domains, locating the SC in the visible range and dynamically tuning the color (*5*–*8*). Otherwise, the maximum reflection of a BCP PC typically occurs at ultraviolet (UV) because of the relatively small period of normal–molecular weight BCPs (*24*–*26*). In most prior work, a swelling agent preferentially absorbed by one of the two BCP domains was used to ensure the mechanical stability of a BCP PC upon swelling (*5*–*8*). A variety of domain swelling agents have been demonstrated, including solvents, ionic liquids, sol-gel precursors, and photocrosslinkable hydrogels, giving rise to visible range SCs of BCP PCs, which are readily changed upon subsequent stimulation (*6*–*8*, *15*, *23*).

To better understand and further control the dynamics of visible SC of a BCP PC upon in and out of a swelling agent, it is crucial to elucidate the structural details of how a swelling agent actually diffuses into a layered PC with alternating solvent-preferential swelling and solvent-excluding nonswelling domains. For a defect-free, one-dimensional (1D) periodic lamellar morphology, solvent ingress would be limited to the side edges of a film, necessitating long times for dynamic SC switching. Moreover, once the swelling agent completely enters across the layers, the topmost layer will "unbind," eventually leading to dissolution of the entire stack into sheet-like micelles. Swelling in a BCP PC is actually quite rapid and does not lead to unbinding, and prior work has suggested that the presence of screw dislocations and a dislocation network within the lamellar stack may provide for the enhanced rates of solvent access (*6*, *7*, *19*). A screw dislocation is a linear defect, and for a 1D BCP lamellar lattice, the Burgers vector is a single period (two layers) directed normal to the layers and parallel to the dislocation line, resulting in a spiral, nonsingular defect that smoothly and continuously connects like-component layers from the top of the film to the bottom and has been assumed without proof as being responsible for the very rapid liquid diffusion during swelling and deswelling of lamellar BCPs (*5*, *27*). Controlled film processing conditions followed by direct visualization of the resultant screw dislocations created during self-assembly of a BCP PC can allow for much improved control of the dynamics of SC evolution when the BCP PC is subsequently exposed to fluid stimuli (e.g., humidity, organic, and ionic liquids).

Here, we directly visualize the presence and influence of screw dislocations in a BCP PC treated with a swelling agent for reversible control of visible SC. The presence of screw dislocations is made evident via two morphological features: (i) direct internal visualization of the screw dislocation core regions and (ii) external topographical surface patterns. The continuous vertical diffusion pathway of the solvent along the spiraling layers in the core region of a screw dislocation of the alternating in-plane poly(styrene) (PS) and quaternized poly(2-vinylpyridine) (QP2VP) lamellae is visualized in a BCP PC in which QP2VP domains are preferentially swollen with an interpenetrated

[1]Department of Materials Science and Engineering, Yonsei University, Seoul 03722, Republic of Korea. [2]Department of Materials Science and Engineering, Texas A&M University, College Station, TX 77843-3003, USA. [3]Department of Chemical and Biomolecular Engineering, Yonsei University, Seoul 03722, Republic of Korea. [4]Department of Chemistry, Research Institute for Natural Sciences Institute of Nano Science and Technology, Hanyang University, Seoul 04763, Republic of Korea. [5]Department of Chemical and Biological Engineering, Korea University, Seoul 02841, Republic of Korea. [6]Division of Life Sciences, Korea University, 145 Anam-Ro, Seongbuk-Gu, Seoul 02841, Republic of Korea. [7]Spin Convergence Research Center, Korea Institute of Science and Technology (KIST), Seoul 02792, Republic of Korea.
*Corresponding author. Email: cmpark@yonsei.ac.kr (C.P.); elt@exchange.tamu.edu (E.L.T.); junehuh@korea.ac.kr (J.H.)
†These authors contributed equally to this work.

hydrogel network. The upper surface of the 1D BCP PC shows concentric wrinkling and bucking when the film is swollen by ethanol, a preferential solvent to QP2VP, followed by complete drying. The characteristic topographical concentric shell pattern emanating from the core region (with both clockwise and counterclockwise concentric spirals) is observed, allowing determination of the spatial locations of vertically oriented screw dislocations. Both upper surface and cross-sectional morphological analysis of a BCP PC film provide a complete 3D description of the diffusion pathway of the solvent.

RESULTS

A 700-nm-thick polystyrene-block-poly(2-vinyl pyridine) (PS-*b*-P2VP) film, comprising alternating in-plane ordered PS and P2VP lamellae, was formed by spin-coating a BCP propylene glycol monomethyl-ether acetate (PGMEA) solution onto a glass substrate. The film was then solvent annealed with chloroform vapor at 60°C for 24 hours to develop a well-defined in-plane orientation of the lamellae. Small-angle x-ray scattering (SAXS) showed a series of peaks corresponding to a basic periodicity of 66 nm (fig. S1). On the basis of the near-symmetric composition, both the PS layers and the P2VP layers are therefore 33 nm thick. A bromoethane/dibromobutane hexane solution was then applied to the film to quaternize and permanently cross-link a fraction of the amine groups in the pyridine rings of the P2VP blocks, as schematically shown in Fig. 1A (fig. S2). Alternating in-plane layers of PS and QP2VP domains were confirmed with bright-field transmission electron microscopy (TEM) (fig. S3), with the alternating QP2VP layers appearing dark because of their preferential staining by I_2. A topmost PS monolayer approximately 16 nm in thickness was also evident, followed by alternating QP2VP and PS bilayers. The image also shows several edge dislocations in the middle of the 1D lamellae stacks (fig. S3). It should be noted that the screw dislocations assumed to act as the pathways for in-and-out solvent diffusion are not observed. This is due to the low probability of encountering the near-core region in a thin cross section of the film used for TEM imaging.

To find and identify a screw dislocation core region, we first prepared a BCP PC with highly swollen but solid QP2VP domains (see Materials and Methods for details) as indicated schematically in Fig. 1A. The sample was prepared using an interpenetrated networked hydrogel (IHN) to swell the pristine BCP PC film, as evident by its reddish SC (see Fig. 1B). We also confirmed that the in-plane lamellar structure of a solid-state BCP PC with IHN-QP2VP domains was well developed over a large area by SAXS (fig. S4). Second, we used a slice-and-view technique where a cross section is obtained by focused ion beam (FIB) milling and observed in situ by scanning electron microscopy (SEM) where the I_2-stained IHN-QP2VP domains appear bright because of the increased secondary electron yield. The sample was then serially sliced in 20-nm steps by FIB, each slice followed by SEM observation, yielding a 3D reconstruction of the dislocation core regions (fig. S5). By systematic cross sectioning over large cross-sectional volumes, a screw dislocation was encountered in the top left [Fig. 1C, (1)], and as the sample was consecutively sliced by the ion beam [Fig. 1C, (1) to (8)] (see movie S1), the curvilinear dislocation core region can be followed downward across many layers. The results indicate that this dislocation line is predominantly of screw character, which is also confirmed by the detailed 3D reconstruction from the SEM images, as shown in Fig. 1D. It should also be noted that our IHN-BCP sample contained line defects that were pure edge dislocations along with edge dislocation loops in addition to the screw dislocations.

To enable TEM observations, once a screw dislocation was evident in slice-and-view SEM, we used the FIB to create a TEM lamella slice of approximately 20-nm thickness containing a portion of the screw dislocation for transfer to a TEM grid for observation of the defect in cross section in bright-field mass thickness TEM. Figure 2A shows the thin unswollen (~30 nm) PS and thick, highly swollen (190 nm), IHN-QP2VP layers giving an overall period of 220 nm, consistent with the value from SAXS (fig. S4). The IHN-BCP PC cross section including a dislocation line unambiguously reveals the origin of the vertical diffusion of a cross-linkable swelling agent, poly(ethylene glycol) diacrylate (PEGDA) oligomer [number-average molecular weight (M_n) = 700 g/mol] across the nonpolar, glassy PS domains. The swollen screw dislocation core size 2rc is taken as the lateral extent of the region where the layers are highly curved and is ~200 nm, comparable with the Burgers vector b in the swollen, 1D crystal. The TEM projection of the 20-nm-thick section sample strongly resembles that of a nonsingular spiral structure like that of a biphasic helicoid, which serves as a continuous pathway for the diffusion of the swelling agent from the top to the bottom of the film (Fig. 2A) (*5*, *6*, *23*, *24*).

The structure of the experimentally observed asymmetrically swollen layers of a preexisting helicoidal defect does not precisely correspond to a helicoidal surface (see Fig. 2B and movie S2) because of the resistance of the glassy PS layers near the core region to decrease their thickness to increase their lateral intermaterial dividing surface (IMDS) area as required by the swelling of the QP2VP layers. However, this defect still exhibits a nonsingular spiral helicoidal defect that smoothly connects like-component layers from the top of the film to the bottom. Unlike screw dislocations in atomic crystals and in smectic liquid crystals, which have distinct, structurally different core regions (for example, in smectic liquid crystals, the dislocation core has a nematic structure) (*28*, *29*), screw dislocations in biphasic 1D periodic soft matter are nonsingular, allowing a swelling fluid to completely bypass a stack of alternating impenetrable A layers by simply following the continuously connected helicoidal spiral of B layers downward and simultaneously outward into the 1D stack, rapidly swelling the set of B layers, giving a quick (~second) shift in visible color over a very large (square centimeter) area. In our 1D BCP material, the crystal and its defects are not defined by precisely positioned atoms or even whole molecules; rather, the crystalline order resides in the periodic structure of the interface between the two block domains (i.e., the IMDS), and as one moves along the IMDS in a given layer and passes near the position of the defect, one can smoothly and continuously follow the layer upward (or downward) without encountering any distinct, abrupt change in the local atomic and molecular packing or in the shape of the IMDS, with no torn edges or other singularities.

To computationally generate a screw dislocation of BCP structure, a BCP molecular model was simulated by a mesoscale density functional theory under the following condition. A lamellar-forming BCP was simulated in a cylindrical volume with a periodic boundary condition imposed in the cylindrical direction (*z* direction). The confining cylindrical wall was modeled to be neutral to both blocks, by which BCP would form an alternate staking of A and B disks along the *z* direction if the cylinder length is commensurate with a natural period. An external force, which would cause a screw dislocation along the cylindrical direction, was applied by imposing a

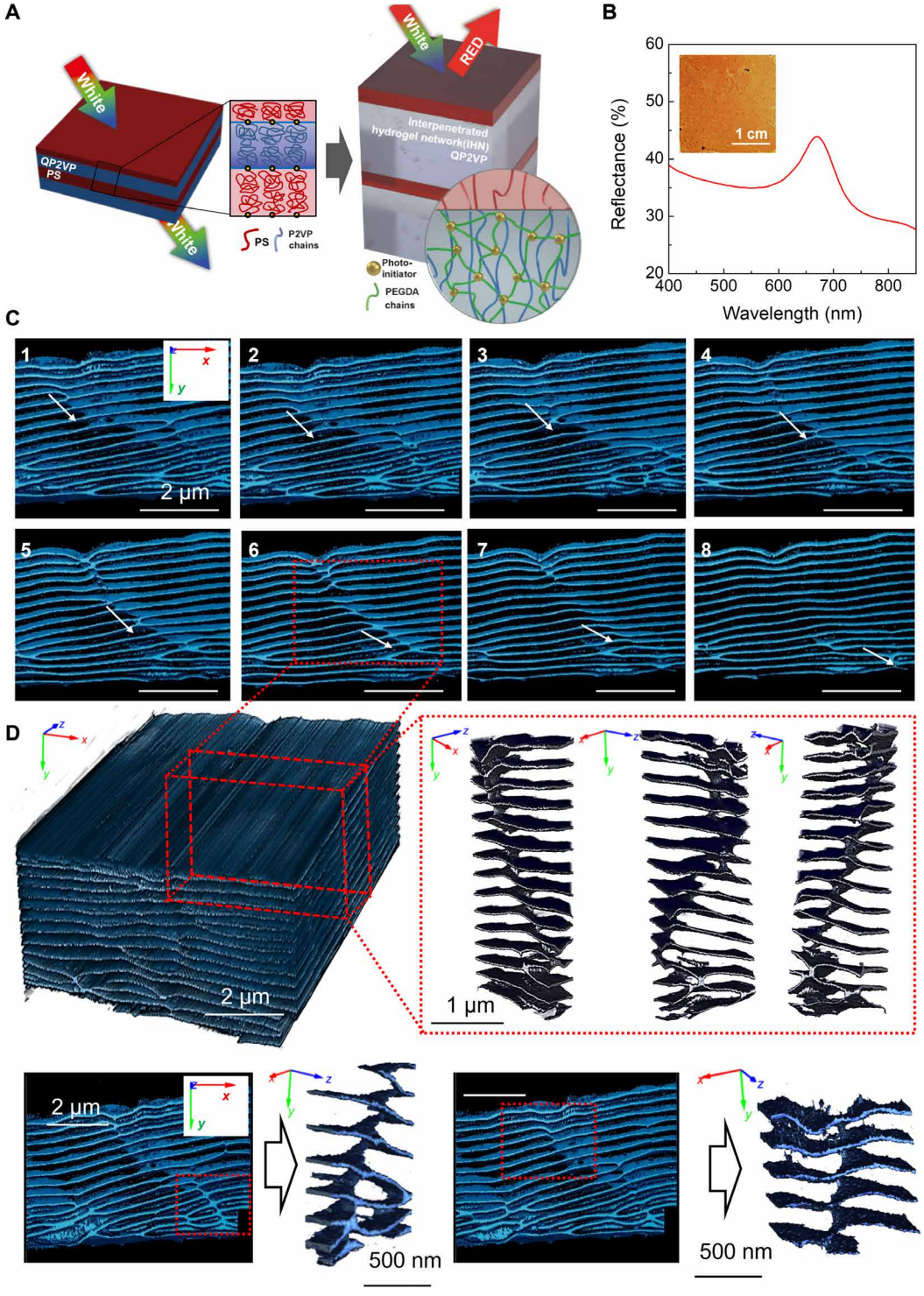

Fig. 1. Screw dislocations in a solid-state BCP PC swollen by hydrogel showing visible SC. (**A**) Schematic illustration of a solid-state PS-*b*-IHN-QP2VP PC having visible range SC. PEGDA, poly(ethylene glycol) diacrylate. (**B**) UV-visible (UV-vis) spectrum of a PS-*b*-IHN-QP2VP film exhibiting red SC. The inset shows a photograph of the film with red SC. (**C**) A series of consecutive slice-and-view field-emission SEM (FE-SEM) images of a PS-*b*-IHN-QP2VP PC with the traces of screw dislocation cores appearing. The orientation of the dislocation cores is indicated by the white single-headed arrows in the photographs. Only PS lamellae were highlighted in blue for visual clarity. (**D**) A 3D reconstructed image (the leftmost) using 226 consecutive FE-SEM images. The *xyz* coordinate indicates that *xy* plane corresponds to the slicing plane, as also shown in the SEM image in (C). The selected regions including image 6 of (C) (a red dotted, rectangular parallelepiped) were highlighted, showing the core of a screw dislocation. Right: 3D views from three different orientations. 3D views including the red dotted boxes in the slice SEM images captured in the movie S1 also show the parts of screw dislocations in the bottom row of (D).

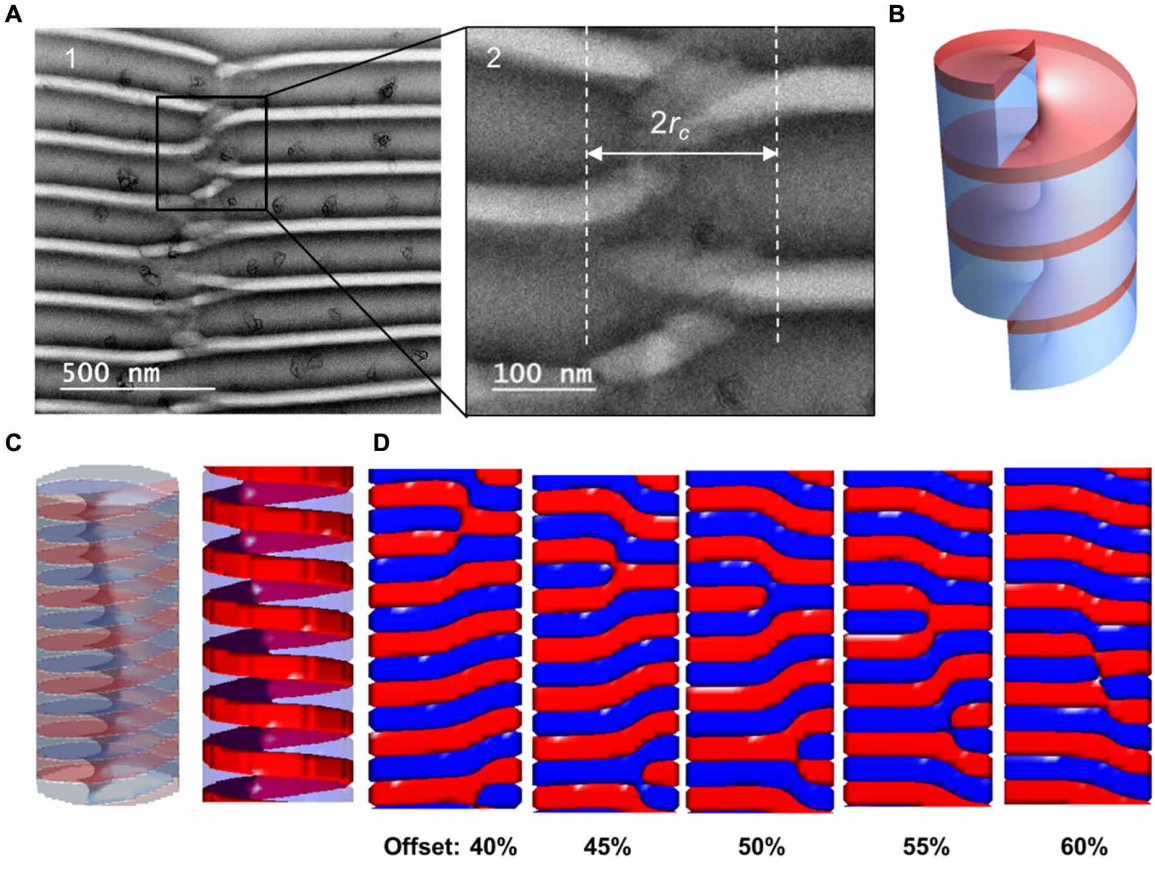

Fig. 2. Direct visualization of a screw dislocation core regions in a solid-state BCP PC. (**A**) Cross-sectional bright-field TEM images of a thin section of containing a screw dislocation. The boxed region in (A1) is magnified in (A2). (**B**) Mathematical model of a nonsingular helicoid structure observed in the stack of lamellar bilayers. The blue domains were rendered translucent for visualizing a core of the screw dislocation. (**C**) A simulated model of a screw dislocation of a BCP consisting of in-plane lamellae with characteristic helical structures obtained by the mesoscale density functional theory. The PS layers are rendered red, and the swollen IHN-QP2VP layers are shown as translucent blue. The rendered results in the right side show the necessity of using TEM with a solid-state BCP PC swollen by hydrogel for direct visualization of a screw dislocation core. (**D**) Cross sections of the simulated helical lamellar structure at various offsets.

condition of incommensurability of BCP natural period with the film thickness. Details of the simulation method are documented in Materials and Methods. Although such incommensurability condition applied on purpose in the simulation does not directly model the small-molecule transport-driven lamellar perturbation in the experimental process, they effectively provide the same means to create a longitudinal force to perturb lamellar structure, which resulted in screw dislocations, as shown in Fig. 2C. The translucent rendering of the domain structure in Fig. 2C revealed that the helix axis of the simulated screw structure is curvilinear. The curvilinear helix axis (dislocation line) in the simulated structure explains how the experimental SEM and TEM images should look like when the cutting plane is at around the core of the helix. The migration of the domain dislocation was evident from layer to layer as the offset progressed (Fig. 2D and movie S3), which corroborates the experimental slice-and-view results in Fig. 1 (C and D).

The locations and areal density of the vertically oriented screw dislocations of the BCP PC film were obtained by examination of the upper film surface morphology after swelling and deswelling of the film with a preferential solvent (Fig. 3A), and the results are shown in Fig. 3. When an initially transparent PS-*b*-QP2VP film is immersed in EtOH, a preferential solvent for QP2VP, the transparent film immediately (within 2 s) turned bluish because of the red shift of its SC arising from the preferential swelling of the QP2VP domains by the EtOH. The SC continuously red-shifted with increasing time and exhibited a red color with the wavelength at the maximum reflectivity asymptotically approaching 700 nm, similar to an IHN-BCP PC (fig. S6). Subsequent drying of the film blue-shifted the SC from red because of the deswelling of the QP2VP lamellae, giving rise to the originally optically transparent film, as shown in a time series of photographs upon swelling and deswelling of the film in Fig. 3B. After complete drying of EtOH, the upper surface of the BCP PC was examined by both SEM and atomic force microscopy (AFM), and the results are shown in Fig. 3 (C and D, respectively). Unique spiral surface patterns were observed centered about screw dislocation cores. A tapping mode (TM) AFM image in Fig. 3D (also see Fig. 3F) shows the topographical spiral patterns with their valley-to-valley repeat distance of approximately 300 nm. The spacing between nearest-neighbor defects varies, with an average distance of ~3 μm, giving rise to a dislocation density of approximately $1 \times 10^{11}/m^2$ as estimated by analysis of a large-area SEM image, as shown in Fig. 3E (fig. S7).

More detailed, finer-scale observation of the periodic topographical spiral patterns with TM-AFM in phase contrast mode revealed the mechanism of the evolution of the patterns via the identification

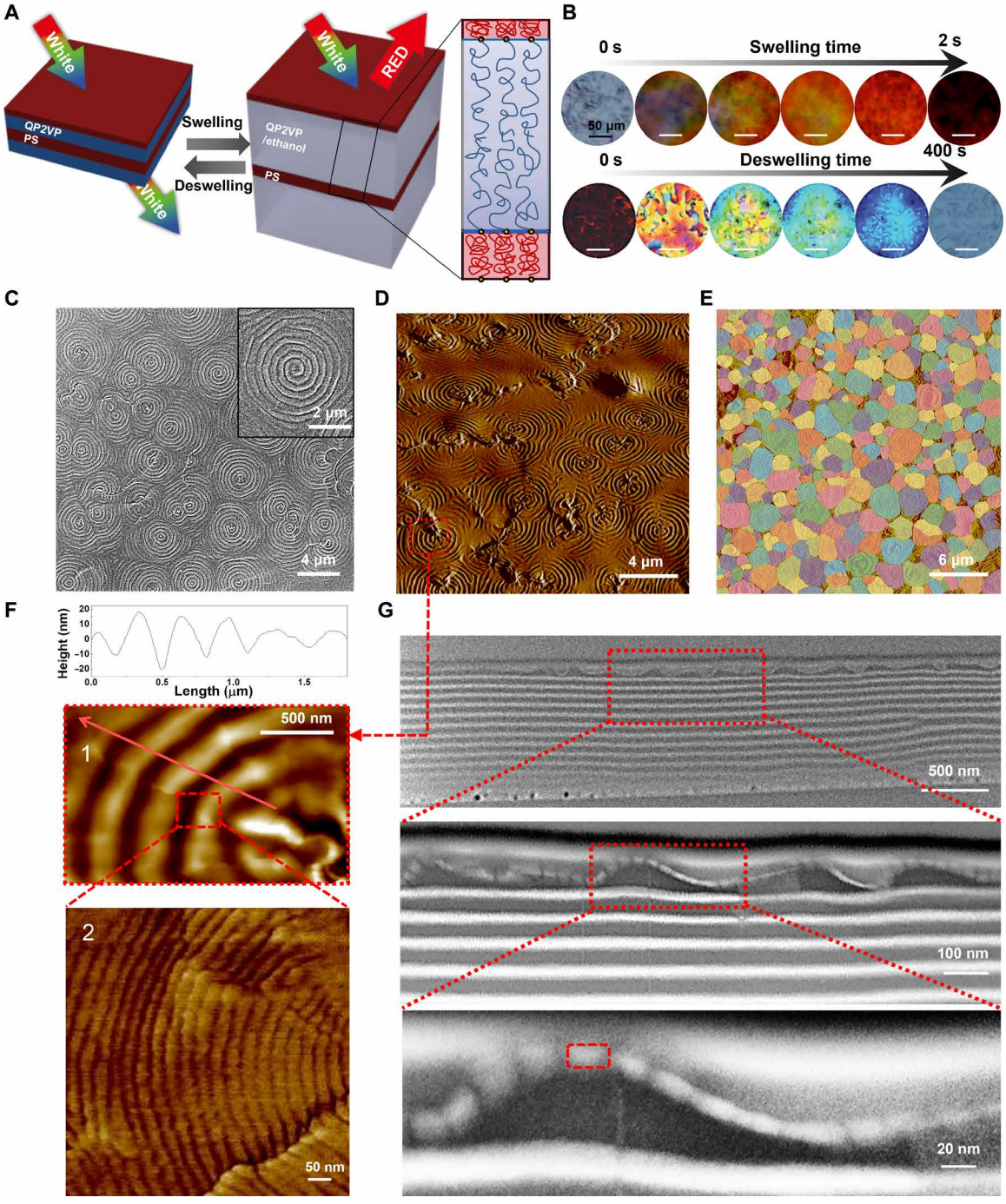

Fig. 3. Visualization of the locations of screw dislocations in a BCP-PC with reversible SC. (**A**) Schematic illustration of the reversible evolution of visible SC in a BCP PC by swelling and deswelling of QP2VP (blue) domains with EtOH. (**B**) A series of photographs showing the initial uneven spatial appearance and disappearance of visible SC of the BCP PC upon swelling and deswelling with EtOH. A FE-SEM (**C**) and AFM (**D**) image of the surface of PS-*b*-QP2VP after swelling by EtOH, followed by deswelling. (**E**) A spatial analysis of the screw dislocations from a large-area AFM image. Different colors were arbitrarily chosen for clear visualization of individual screw dislocations. There are approximately 0.1 screw dislocations per square micrometer. (**F**) An AFM image in height contrast magnified in the red box regions of (D). The height surface profile along the direction of the red arrow in the top image (F1) is shown. A magnified AFM image in phase contrast mode shows the detail within the red dotted box in the bottom (F2) image. (**G**) Cross-sectional TEM images with increasing magnification of a PS-*b*-QP2VP film dried after swelling by EtOH. The buckled top layer of surface-reconstructed PS/QP2VP is apparent. The images in the red boxes show alternating wide PS and narrow QP2VP regions in the buckled top layer.

of another pseudo-periodic but finer-scale circular surface pattern with a periodicity of approximately 40 nm, as shown in image 2 in Fig. 3F. The upper surface was initially nearly flat after solvent casting, annealing, and quaternization (fig. S8), and the fine-scale structure only appeared after solvent swelling and deswelling. A cross-sectional TEM image reveals that the topmost PS layer exhibits the 300-nm periodicity after the swelling and deswelling with EtOH (see Fig. 3G), consistent with the AFM observation in Fig. 3 (D and F). Furthermore, careful inspection shows that the topmost PS layer has fractured and then surface-reconstructed, giving rise to alternating PS and QP2VP regions. The two-length-scale (40 and 300 nm), periodic topographical pattern on the BCP PC film thus arises from the interplay of a screw dislocation of the BCP PC with the top glassy PS layer deformations caused by the in-and-out diffusion of EtOH. The periodic surface structure was repetitively observed upon consecutive swelling and deswelling events (fig. S6).

The screw dislocations are assumed to occur upon the relaxation of Burgers vector resulting from imperfect commensurability of the alternating lamellae on a substrate during film preparation steps. The screw dislocations may form during the initial nucleation and growth of the lamellar film and/or they may form during the annealing. The order of flat parallel lamellae in a film is presumably not good initially and then as the layers lower their free energy by becoming more parallel, uniform, and flat with solvent annealing. During solvent annealing, the distortions and angular variations of the misaligned lamellae are localized into dislocation core regions. Several BCP samples were prepared and subsequently solvent-annealed in chloroform with different time periods. The samples were then quaternized, and subsequently swollen in ethanol, followed by drying. The screw dislocations whose cores were exposed to the film surface were determined by the characteristic buckled surface texture as a function of solvent annealing time, and the results are shown in fig. S9. As expected, screw dislocations associated with the surface buckling during solvent swelling and deswelling were rarely visible in an as-cast film because of the lack of the ordering of the in-plane lamellae. The number of screw dislocations abruptly increased with solvent annealing for 1 min. The screw dislocations were rarely altered in number after 24-hour solvent annealing.

Thus, when a BCP PC film is covered with a swelling solvent, the liquid accesses the interior region of the film via the vertically oriented screw dislocations by entering into the interconnected solvent-favorable QP2VP layers below the nonswellable topmost PS layer. Solvent travels inward following the QP2VP component spiraling around the nonsingular core region of a screw dislocation and diffusing radially outward, swelling each QP2VP layer. The less constrained regions away from the core bulge out since the QP2VP layer near the core swells less than the outer regions because of the constraint by the connected glassy PS layers (*30*, *31*), as shown in Fig. 4. This connectivity also prevents unbinding of successive layers. Because of the approximately axisymmetric swelling of the adjacent QP2VP layer, the glassy topmost PS half layer periodically fractures in the outward radial directions from the dislocation core. During the swelling, the areas in-between the circumferentially broken PS domain are filled with QP2VP chains, giving rise to an expanded upper layer with increased area due to the alternating PS/QP2VP regions. Upon evaporation of EtOH, the underlying QP2VP layers contract and the enlarged reconstructed upper surface mechanically buckles, leading to the spiral and concentric ring patterns, as observed in Fig. 3 (C, D, and F).

The swelling of QP2VP domains upon exposure to either monomers of interpenetrated hydrogel network or ethanol occurred because of the preferential molecular interaction between QP2VP chain and a swelling agent involving the rapid diffusion of the agent through screw dislocations. To theoretically examine the molecular interaction of QPVP with various solvents, we computed the solvation free energy of Q2VP trimer in various solvents [water, PEGDA, methanol (MeOH), ethanol (EtOH), 1-propanol (PrOH), and 1-butanol (BtOH)], which allows us to compare the solvation power of those solvents for QP2VP. As seen in the figure below (fig. S10), the solvation free energies of Q2VP trimer suggests that Q2VP interacts more favorably with alcohols than water or PEGDA. This may reflect more alcohol-like structure of Q2VP monomer consisting of nonpolar ethyl groups and polar pyridine having a quaternized ring nitrogen, which leads to a more favorable attraction with alkyl alcohols than water. The respective molecular geometries are depicted in fig. S11. To confirm the swelling arising from the preferential molecular interaction of QP2VP with a swelling agent, we examined the surface of a BCP PC film upon swelling and deswelling of QP2VP domains with different solvents such as propanol and butanol, and the results are shown in fig. S12. The characteristic surface texture arising from the surface buckling upon swelling and deswelling was observed with both propanol and butanol, which implies the preferential interaction of QP2VP with those solvents. The speed of SC evolution is mainly governed by the density of screw dislocations in a film with a given swelling agent. The literature shows that interlayer diffusion in a smectic liquid crystal through screw dislocations is proportional to the areal density of the screw dislocations (*29*). We speculate that in principle, the higher and more uniform the areal density of the screw dislocations, the faster the switching speed. However, the quality of reflection of the film became worse as the areal density increased. One plausible way to resolve this trade-off is to micro- or nanopattern a BCP PC film. In a patterned PC film, where thin regions are removed, a swelling agent can diffuse into QP2VP domains not only through a screw dislocation but also directly into each layer via the sides of the pattern with exposed QP2VP domains.

The mechanical loading situation can be approximated as that of a bilayer, composed of a hard, thin, upper layer on top of a thick prestrained elastomeric layer in which buckling of the hard layer occurs when the prestrain is released in the elastomer (fig. S13) (*32*–*35*). On the basis of the morphological information of the buckled structures shown in table S1 (Supplementary Materials) including the valley-to-valley periodicity (λ_0 = ~300 nm), amplitude of a valley (A_0 = ~50 nm), and thickness of the topmost PS layer (h = ~16 nm), the strain of the topmost PS layer upon solvent swelling was calculated with the theoretical equations $\lambda_0 = \frac{\pi h}{\sqrt{\varepsilon_c}}$ and $A_0 = h\sqrt{\frac{\varepsilon_{pre}}{\varepsilon_c} - 1}$ developed for bilayer buckling of prestrained elastomer/hard layer. First, the critical strain (ε_c) was obtained with using the first expression and the value was approximately 0.03. The prestrain (ε_{pre}) in the following equation, which corresponded to the strain exerted to the enlarged topmost layer was approximately 30%. The reconstructed topmost layer in Fig. 3G shows that the QP2VP domains of approximately 10 nm alternate with wider 30-nm PS regions. The total area of the QP2VP domains corresponds to approximately 30% of the pristine PS layer, consistent with the calculation results.

The ratio of Young's modulus of the reconstructed layer (E_{eff}) to the underneath QP2VP gel ($E_{QP2VP-gel}$) was obtained from the

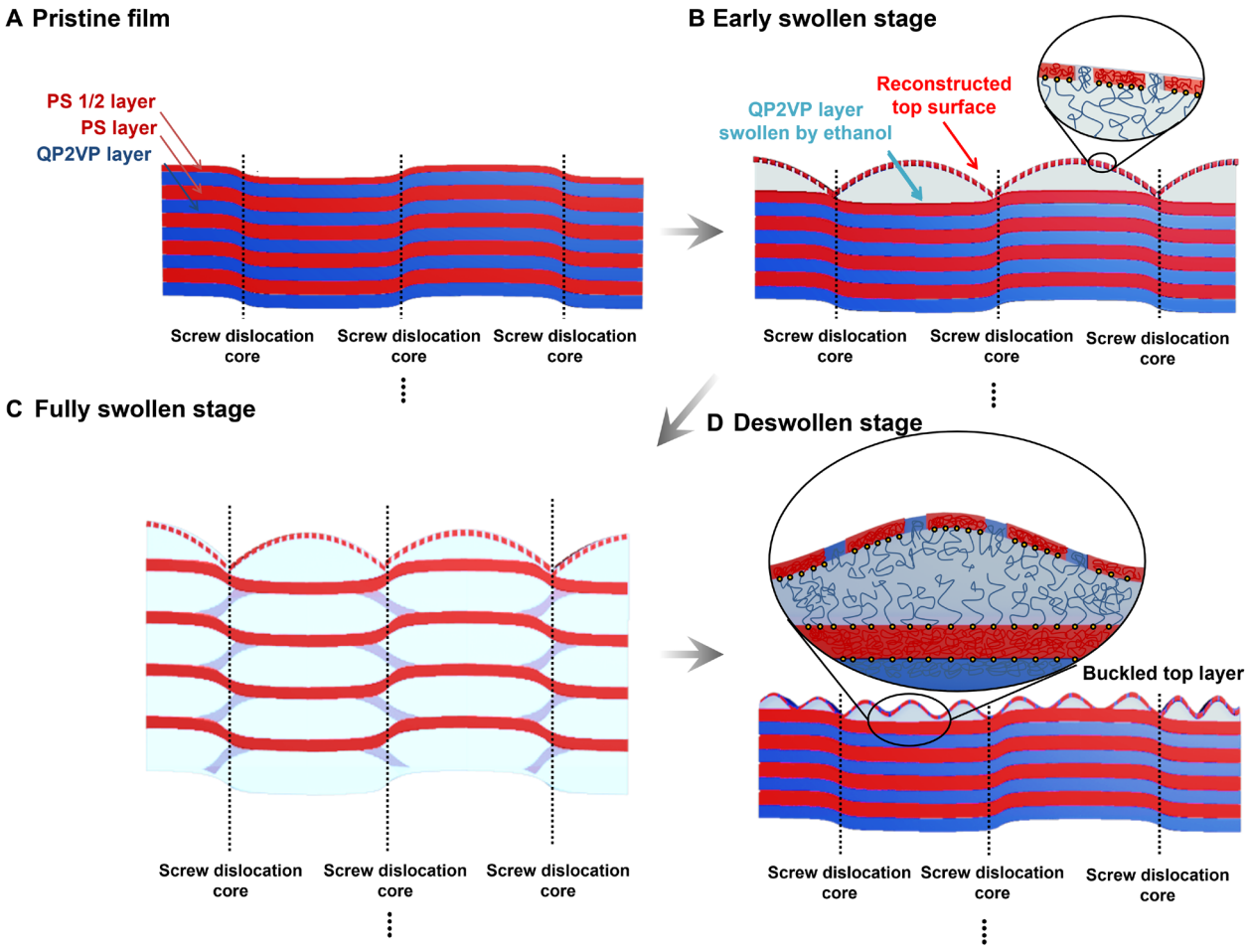

Fig. 4. The mechanism of fracture of the topmost PS layer of a BCP PC upon solvent swelling and deswelling. (**A**) PS, QP2VP, and QP2VP swollen by EtOH are represented with the colors of red, blue, and sky blue, respectively. (**B**, **C**) The uppermost single PS brush layer undergoes biaxial tensile fracture during swelling, and some QP2VP blocks penetrate into these circular cracks. (**D**) Upon deswelling, the extended PS plus QP2VP-filled regions in the upper layer cannot relax back to its original area and thus displays a wrinkled upper surface.

equation of $\varepsilon_c = 0.52\left[\frac{E_{QP2VP-gel}(1-\nu_{eff}^2)}{E_{eff}(1-\nu_{QP2VP-gel}^2)}\right]^{2/3}$, where ν_{eff} and $\nu_{QP2VP-gel}$ are Poisson ratio of the reconstructed top layer and bottom QP2VP layer, respectively. With the assumption of ν_{eff} and $\nu_{QP2VP-gel}$ of approximately 0.3 and 0.5 corresponding to the values for glassy and rubbery layer, respectively (table S1) (*36*), the $E_{QP2VP-gel}/E_{eff}$ was approximately 0.01. Effective Poisson ratio of top layer after swelling-deswelling cycles was obtained from the rule of mixture $\nu_{eff} = V_{PS}\nu_{PS} + V_{P2VP}\nu_{P2VP}$. Effective Young's modulus of top layer (E_{eff}) after swelling-deswelling cycles from rule of mixture was obtained of approximately 3 GPa by the relation of $E_{eff} = V_{PS}E_{PS} + V_{P2VP}E_{P2VP}$. The estimated $E_{QP2VP-gel}$ was approximately 40 MPa, which is in good agreement with the value of a typical elastomer (*23*). We also calculated the maximum height of a swollen screw dislocation upon EtOH swelling based on the scheme in fig. S13. With the average radius of screw dislocations of approximately 1.5 μm, the height of a swollen screw dislocation core was approximately 1 μm, comparable with those observed in highly swollen BCP PCs. Remarks should be added about the fact that the 2D surface-buckled structure observed in a PS-*b*-QP2VP film after EtOH swelling and deswelling is not modeled precisely by the 1D bilayer model. It should be noted that the theories are rarely developed on the buckling in biaxially prestrained bilayers, while several theories exist of a uniaxially prestrained bilayer (*37*). The recent study shows that the buckling behavior in a biaxially prestrained bilayer is similar to that of a uniaxially prestrained bilayer (*38*).

Our speculation based on the radial surface reconstruction of a topmost PS layer into one with alternating PS/QP2VP domains from the cores of screw dislocations was indirectly confirmed by fabricating micrometer-scale film patterns of a BCP PC film by reactive ion etching (RIE) (Fig. 5A), and the results are shown in Fig. 5. When a BCP PC film was immersed in EtOH, primary diffusion pathways for EtOH to come into the film were dislocation cores randomly distributed on the film surface. The lateral diffusion of EtOH that happened only at the edges of a film would rarely affect the development of the surface reconstruction of a topmost PS layer near each core of screw dislocation. To make the solvent diffusion through film edges more dominant than that through the screw dislocations, we fabricated micropatterned BCP PC film in which lateral diffusion could be facilitated through the edges of the small micropatterned domains. Representative, arrays of hexagonal BCP PC patterns of approximately 10 μm in width were developed with *p6mm* symmetry, as shown in Fig. 5 (B and C①). The micropatterns were subsequently immersed

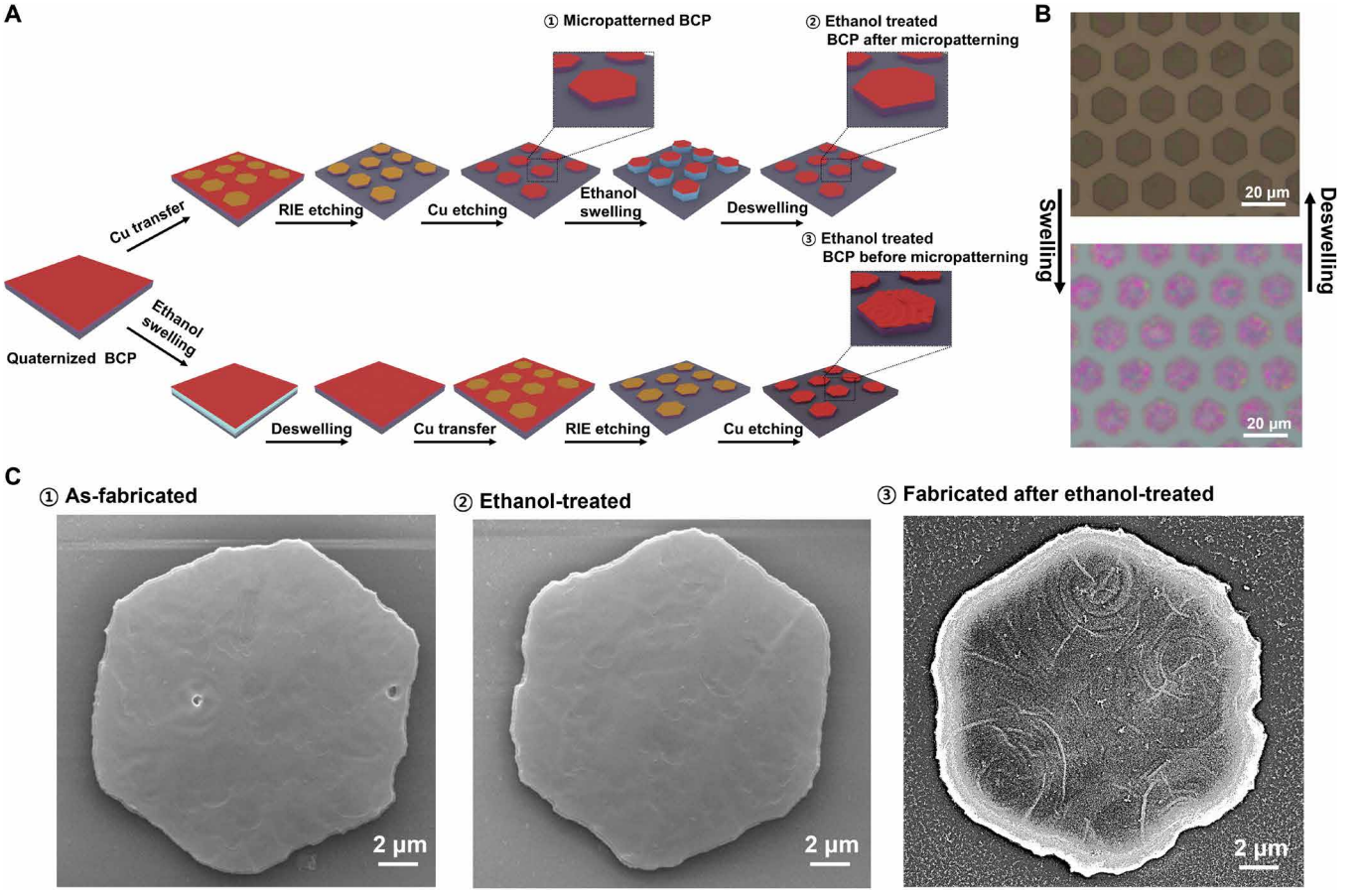

Fig. 5. Surface characteristics of a micropatterned BCP PC film upon swelling and deswelling. (**A**) Schematic illustration of the fabrication process for a micropatterned PS-*b*-QP2VP PC with two different routes for EtOH swelling and deswelling. (**B**) An optical microscope image of micropatterned PS-*b*-QP2VP film in the step A ③ of (A) during swelling and deswelling process. Notably, an optical microscope image similar to (B) was also observed in the step A ② of A. (**C**) FE-SEM images of single hexagonal piece of PS-*b*-QP2VP. A hexagon with flat surface of an as-fabricated pattern was obtained in the step ① of (A). In C②, after ethanol swelling and deswelling, the surface remains flat. However, when the hexagonal piece is fabricated after a large-area PS-*b*-QP2VP PC film was swollen and deswollen, a typical hexagonal piece shows that the upper surface has patterns due to film buckling from swelling-deswelling stresses. The location of the characteristic screw dislocations is at the center of the concentric rings. Vertically oriented screw dislocations of a 1D lamellar-forming BCP PC are reconstructed, which facilitate the rapid response of its stimuli-interactive SC in visible range. Direct visualization confirms that the dislocations are low-energy helicoidal screw dislocations having unique, nonsingular cores, enabling understanding of the dynamics of BCP SC.

into EtOH to develop the characteristic red SC of the arrays (Fig. 5B), followed by being completely dried. The ordered surface structures were hardly observed on the micropatterned BCP films, as shown in Fig. 5C②. Because EtOH dominantly diffused through the micrometer-scale edges of each hexagonal film rather than exclusively through cores of dislocations, as shown in the cross-sectional image of a hexagon in the right SEM image of Fig. 5C②, radial stressing of the topmost PS layer of each hexagonal film rarely occurred. On the other hand, a BCP PC film, which had been immersed in EtOH, followed by drying was subsequently micropatterned. The ordered surface structure was observed on the patterned domains (Fig. 5C③), which confirms the role of the lateral diffusion of EtOH into the hexagonal piece with stress-free edges of the topmost PS film.

DISCUSSION

In summary, vertically oriented screw dislocations in a self-assembled BCP PC consisting of in-plane lamellae provided continuous rapid in-and-out diffusion of a preferential swelling agent to one of the layers for controlling the visible range SC of the film allowing rapid sensing. The vertically oriented nonsingular helicoidal defects were directly visualized by 2D TEM projections and slice-and-view SEM 3D reconstructions in a highly swollen but solid IHN-BCP PC film with visible SC. A nanometer-scale circular pattern of the topmost glassy PS layer develops about each dislocation, arising from surface buckling and allows visualization of the location and areal density of the screw dislocations. Both cross-sectional and surface morphological analyses provide a complete 3D description of the rapid diffusion pathways of the swelling agent in the BCP PC. The detailed nature of the screw dislocation core structure plays a critical role on the efficient interlayer diffusion in various 1D periodic materials including smectic liquid crystals (*28*, *29*), 2D layered crystals (*39*), and nanoporous materials (*40*). Thus, engineering of such valuable defects via substrate patterning (*41*–*43*) suggests future designs for purposeful defect-containing layered materials to enhance the dynamics of SC suitable for emerging stimuli-interactive SC sensors and displays.

MATERIALS AND METHODS

Material

A PS-*b*-P2VP was synthesized via living anionic polymerization in tetrahydrofuran at −78°C with the initiator *sec*-butyllithium (*44*). The average molecular weight of the PS-*b*-P2VP BCP was 126 kg mol^{-1} [Φ_{ps} = 0.49 and polymer dispersity index (PDI) = 1.05] (*44*). For the fabrication of BCP PC films, PGMEA, chloroform, bromoethane, and 1,4-dibromobutane and the solvents for swelling the BCP film, such as ethanol, propanol, and butanol, as well as PEGDA (M_n = 700), 2-hydroxy-2-methylpropiophenone (HOMPP), and Triton X-100 to make the solid-state BCP PC SC film, were purchased from Sigma-Aldrich. Poly (dimethylsiloxane) (PDMS) prepolymer (Sylgard 184) and the curing agent were purchased from Dow Corning for patterning of BCP PC film.

Fabrication of PC films

BCP PC films were prepared via spin coating with 7 weight % (wt %) PS-*b*-P2VP solutions in PGMEA onto a glass substrate to make a BCP film thickness of 700 nm. Then, the films were solvent-annealed at 60°C for 24 hours in chloroform vapor. After that, the films were soaked in hexane solution with1-bromoethane and 1,4-dibromobutane at 60°C for 24 hours, making P2VP layers in the films that were selectively quaternized. The amount of the cross-linker 1,4-dibromobutane controls the SC of a BCP PC film (*6*, *7*).

Micropatterning of BCP PC film

For micropatterning hexagonal arrays of a BCP PC film, a PDMS mold with hexagonal mesas of approximately 10 μm in size in *p6mm* symmetry was used. The PDMS mold was obtained by curing a PDMS precursor with thermal cross-linker poured on a prepatterned Si master mold with 60°C for 12 hours. A thin Cu film was coated on the surface of the PDMS mold by thermal evaporation. The Cu layer on the mesas of the PDMS pattern was selectively transferred onto the BCP PC film using contact printing with gentle pressure for 5 min, giving rise to hexagonally patterned Cu film on the BCP PC. The oxygen RIE was performed on the BCP PC film with Cu pattern, which served as a pattern mask for RIE, in inert argon atmosphere. Sequentially, the Cu mask was removed by immersing it in ammonium persulfate solution.

Preparation of a swollen solid-state BCP PC film with IHN

A highly swollen BCP PC film was prepared as a dry solid using an IHN in the pristine PS-*b*-QP2VP BCP PC film (*23*). PEGDA (M_n = 700) (~50 wt % in water) was blended with Triton X-100 at a concentration of 1 wt %. Triton X-100 was used to control the wettability and diffusion rate to make PEGDA uniformly swell the QP2VP layers. The HOMPP was also added to the blend solution at a concentration of 1.5 wt % for cross-linking the PEGDA chains. The mixture of PEDGA, Triton X-100, and HOMPP was spread onto the surface of a BCP PC film, allowing diffusion into the QP2VP domains. The swollen PS-*b*-QP2VP film with the hydrogel oligomers and initiators was then irradiated with UV (wavelength of 350 nm) for a certain time, followed by rinsing of the unreacted, residual oligomer, giving rise to IHNs in the QP2VP domains (see fig. S2). By controlling the UV irradiation time, we were able to develop a solid-state BCP PC film with its red SC. For FIB-SEM and TEM characterization of the IHN-BCP film, the film was further dried at 60°C for 6 hours on a hot plate to remove the residual water.

Characterization

The surface morphologies of BCP PC films were examined by TM-AFM (Nanoscope Iva Digital Instruments) in height and phase modes and field-emission SEM (FE-SEM) (JEOL-7001F) with an accelerating voltage of 15.0 kV. The cross-sectional morphologies of the BCP PCs were characterized by bright-field TEM using iodine staining to increase the scattering of the QP2VP layers (the PS layers therefore appear light in bright-field TEM images) with spherical aberration-corrected scanning TEM (STEM) (JEM-ARM 200F, JEOL, with an accelerating voltage of 200 kV). FIB slicing and scanning electron beam imaging (FIB-SEM) (Helios 5 UC, FEL) used a Ga^+ ion accelerating voltage (30 kV) and ion current (0.23 nA) with an estimated slice thickness of ~20 nm. The electron beam voltage was 2.00 kV with a beam current of 0.5 nA. Because of the iodine staining, the wider, swollen IHN-QP2VP layers appear brighter in the secondary electron images than the thin, nonswollen dark PS layers. The STEM samples were prepared with a FIB (JIB-4601F, JEOL). The nanostructures of BCP PCs were characterized by both transmission SAXS and 2D grazing incidence SAXS at PLS-II 9A U-SAXS beamline (Pohang Accelerator Laboratory) with a 2D charge-coupled device detector (Rayonix SX165, USA) and *d* spacing from 10 to 400 nm. UV-visible (UV-vis) spectra of BCP PCs were obtained with a UV-vis spectrometer (Cary 5000, Agilent). The micropatterned films pieces of the BCP PCs were observed by an optical microscope (BX 51M, Olympus).

Model for screw dislocation of biphasic structure

The screw dislocations of biphasic lamellae were modeled by the equation of helicoid in cylindrical coordinates (r, ϕ, and z), which can be expressed in terms of three parameters, r, ϕ, and t by

$$(x, y, z) = (r\cos\phi, r\sin\phi, c\phi + ft) \quad (1)$$

$$(x, y, z) = (r\cos\phi, r\sin\phi, c\phi - (1 - f)t) \quad (2)$$

where f is the fraction of one of the lamellar domains [we take f = 0.15 (PS), therefore $1 - f = 0.85$ (corresponding to 6:1 swollen QP2VP)]. The parameters r, ϕ, and t are in the range of

$$0 \le r \le D/2, 0 \le \phi \le 2n\pi, 0 \le t \le 2c\pi \quad (3)$$

Here, D is the outer diameter of helicoid and n is the number of turns, and $2c\pi$ is the pitch of the helicoid. The screw dislocation of biphasic lamellae shown in Fig. 2B is depicted using Mathematica 12.0 (Wolfram Research Inc.) with the values of $D = 4$, $n = 3$, $c = 1/3$, and $f = 0.15$.

3D reconstruction from multiple SEM images

A volume of 4600 nm by 1200 nm by 5400 nm BCP film with a voxel size of 5 nm by 5 nm by 20 nm was reconstructed from 226 SEM images by volume rendering using MATLAB R2020b.

Molecular simulation of BCP lamellae with screw dislocations

The lamellar morphology of AB diblock copolymer melt was simulated in a cylindrical volume with a periodic boundary condition imposed in the cylindrical direction (z direction). The confining cylindrical wall was modeled to be neutral to both blocks, by which BCP would form an alternate staking of A and B disks along the z direction if the cylinder length is commensurate with a natural period. For incommensurate conditions, on the other hand, a longitudinal force is created because of the period mismatch and perturbs

the lamellar disks, resulting in tilted disks or helical lamellar structure. Landau-Ginzburg approach was used with the Cahn-Hilliard-Cook diffusion equation for the evolution BCP morphology (*45*, *46*)

$$\frac{\partial \psi(\mathbf{r})}{\partial t} = M\nabla^2\left(\frac{\partial(F + F_{\text{surf}})}{\partial \psi}\right) + \xi(\mathbf{r}) \quad (4)$$

Here, the order parameter ψ describes the deviation of local A-monomer fraction from its average value at a position **r** [defined by $\psi(\mathbf{r}) = \varphi(\mathbf{r}) - \varphi$, where $\varphi(\mathbf{r})$ and φ are the local fraction of A-monomer and the mean fraction of A-monomer], M is a mobility constant set to be unity, F is the free energy functional of the BCP, F_{surf} is the free energy associated with interaction between surface of confined geometry and BCP, and ξ represents the thermal noise. The free energy functional, F, is given approximately by Landau-type free energy

$$F(\psi) \cong \int d\mathbf{r}\left[-\frac{\tau}{2}\psi^2(\mathbf{r}) + \frac{\mu}{3!}\psi^3(\mathbf{r}) + \frac{\lambda}{4!}\psi^4(\mathbf{r}) + \frac{D}{2}\{\nabla\psi(\mathbf{r})\}^2\right] + \frac{b}{2}\int d\mathbf{r}_1 \int d\mathbf{r}_2\, G(\mathbf{r}_1 - \mathbf{r}_2)\,\psi(\mathbf{r}_1)\,\psi(\mathbf{r}_2) \quad (5)$$

Here, τ is a temperature-like parameter related to the Flory interaction parameter between A- and B-monomer (χ), μ, and λ and is related to the architecture of BCP determining conformational contributions, and the last term represents a long-range repulsion penalizing long-wavelength inhomogeneity through the Green function G with a period-controlling parameter b. For lamellar-forming BCP, the molecular parameters in Eq. 5 are set to be $\tau = 0.1$, $\mu = 0.0$, $\lambda = 1.566$, $D = 0.333$, and $b = 0.0144$, respectively (*46*). The surface free energy F_{surf} is set to be zero so that the cylindrical wall is neutral to both blocks. The diffusion equation of Eq. 4 is numerically integrated in the discrete space with the boundary condition for a cylindrical geometry of confinement.

SUPPLEMENTARY MATERIALS

Supplementary material for this article is available at https://science.org/doi/10.1126/sciadv.abm5120

REFERENCES AND NOTES

1. E. Yablonovitch, Photonic band-gap structures. *J. Opt. Soc. Am. B* **10**, 283–295 (1993).
2. Y. Fink, J. N. Winn, S. Fan, C. Chen, J. Michel, J. D. Joannopoulos, E. L. Thomas, A dielectric omnidirectional reflector. *Science* **282**, 1679–1682 (1998).
3. A. Urbas, R. Sharp, Y. Fink, E. L. Thomas, M. Xenidou, L. J. Fetters, Tunable block copolymer/homopolymer photonic crystals. *Adv. Mater.* **12**, 812–814 (2000).
4. J. H. Lee, C. Y. Koh, J. P. Singer, S. J. Jeon, M. Maldovan, O. Stein, E. L. Thomas, 25th anniversary article: Ordered polymer structures for the engineering of photons and phonons. *Adv. Mater.* **26**, 532–569 (2014).
5. Y. Kang, J. J. Walish, T. Gorishnyy, E. L. Thomas, Broad-wavelength-range chemically tunable block-copolymer photonic gels. *Nat. Mater.* **6**, 957–960 (2007).
6. H. S. Kang, J. Lee, S. M. Cho, T. H. Park, M. J. Kim, C. Park, S. W. Lee, K. L. Kim, D. Y. Ryu, J. Huh, E. L. Thomas, C. Park, Printable and rewritable full block copolymer structural color. *Adv. Mater.* **29**, 1700084 (2017).
7. H. Eoh, H. S. Kang, M. J. Kim, M. Koo, T. H. Park, Y. Kim, H. Lim, D. Y. Ryu, E. Kim, J. Huh, Y. Kang, C. Park, Nonvolatile, multicolored photothermal writing of block copolymer structural color. *Adv. Funct. Mater.* **29**, 1904055 (2019).
8. T. J. Park, S. K. Hwang, S. Park, S. H. Cho, T. H. Park, B. Jeong, H. S. Kang, D. Y. Ryu, J. Huh, E. L. Thomas, C. Park, Electrically tunable soft-solid block copolymer structural color. *ACS Nano* **9**, 12158–12167 (2015).
9. J. J. Walish, Y. Kang, R. A. Mickiewicz, E. L. Thomas, Bioinspired electrochemically tunable block copolymer full color pixels. *Adv. Mater.* **21**, 3078–3081 (2009).
10. K. Hwang, D. Kwak, C. Kang, D. Kim, Y. Ahn, Y. Kang, Electrically tunable hysteretic photonic gels for nonvolatile display pixels. *Angew. Chem. Int. Ed.* **50**, 6311–6314 (2011).
11. Y. Lu, H. Xia, G. Zhan, C. Wu, Electrically tunable block copolymer photonic crystals with a full color display. *J. Mater. Chem.* **19**, 5952–5955 (2009).
12. Y. Lu, C. Meng, H. Xia, G. Zhang, C. Wu, Fast electrically driven photonic crystal based on charged block copolymer. *J. Mater. Chem. C* **1**, 6107–6111 (2013).
13. M. Shan, X. Ni, J. Xu, Y. Cao, Amphiphilic copolymer self-assembly of magnetic nanoparticles for construction of magnetically responsive photonic crystals based on steric hindrance. *RSC Adv.* **9**, 41280–41286 (2019).
14. Q. He, K. H. Ku, H. Vijayamohanan, B. J. Kim, T. M. Swager, Switchable full-color reflective photonic ellipsoidal particles. *J. Am. Chem. Soc.* **142**, 10424–10430 (2020).
15. T. H. Park, H. Eoh, Y. Jung, G.-W. Lee, C. E. Lee, H. S. Kang, J. Lee, K.-B. Kim, D. Y. Ryu, S. Yu, C. Park, Thermo-adaptive block copolymer structural color electronics. *Adv. Funct. Mater.* **31**, 2008548 (2021).
16. D.-P. Song, C. Li, N. S. Colella, X. Lu, J.-H. Lee, J. J. Watkins, Thermally tunable metallodielectric photonic crystals from the self-assembly of brush block copolymers and gold nanoparticles. *Adv. Optical. Mater.* **3**, 1169–1175 (2015).
17. Y. Ahn, E. Kim, J. Hyon, C. Kang, Y. Kang, Photoresponsive block copolymer photonic gels with widely tunable photosensitivity by counter-ions. *Adv. Mater.* **24**, OP127–OP130 (2012).
18. E. Kim, C. Kang, H. Baek, K. Hwang, D. Kwak, E. Lee, Y. Kang, E. L. Thomas, Control of optical hysteresis in block copolymer photonic gels: A step towards wet photonic memory films. *Adv. Funct. Mater.* **20**, 1728–1732 (2010).
19. T. H. Park, S. Yu, S. H. Cho, H. S. Kang, Y. Kim, M. J. Kim, H. Eoh, C. Park, B. Jeong, S. W. Lee, D. Y. Ryu, J. Huh, C. Park, Block copolymer structural color strain sensor. *NPG Asia Mater.* **10**, 328–339 (2018).
20. E. P. Chan, J. J. Walish, E. L. Thomas, C. M. Stafford, Block copolymer photonic gel for mechanochromic sensing. *Adv. Mater.* **23**, 4702–4706 (2011).
21. C.-H. Cheng, S. Masuda, S. Nozaki, C. Nagano, T. Hirai, K. Kojio, A. Takahara, Fabrication and deformation of mechanochromic nanocomposite elastomers based on rubbery and glassy block copolymer-grafted silica nanoparticles. *Macromolecules* **53**, 4541–4551 (2020).
22. I. R. Howell, C. Li, N. S. Colella, K. Ito, J. J. Watkins, Strain-tunable one dimensional photonic crystals based on zirconium dioxide/slide-ring elastomer nanocomposites for mechanochromic sensing. *ACS Appl. Mater. Interfaces* **6**, 3641–3646 (2015).
23. H. S. Kang, S. W. Han, C. Park, S. W. Lee, H. Eoh, J. Baek, D.-G. Shin, T. H. Park, J. Huh, H. Lee, D.-E. Kim, D. Y. Ryu, E. L. Thomas, W.-G. Koh, C. Park, 3D touchless multiorder reflection structural color sensing display. *Sci. Adv.* **6**, eabb5769 (2020).
24. A. Noro, Y. Tomita, Y. Matsushita, E. L. Thomas, Enthalpy-driven swelling of photonic block polymer films. *Macromolecules* **49**, 8971–8979 (2016).
25. M. Appold, E. Grune, H. Frey, M. Gallei, One-step anionic copolymerization enables formation of linear ultrahigh-molecular-weight block copolymer films featuring vivid structural colors in the bulk state. *ACS Appl. Mater. Interfaces* **10**, 18202–18212 (2018).
26. J. Yoon, W. Lee, E. L. Thomas, Highly oriented thin-film microdomain patterns of ultrahigh molecular weight block copolymers via directional solidification of a solvent. *Adv. Mater.* **18**, 2691–2694 (2006).
27. Y. Fan, J. J. Walish, S. Tang, B. D. Olsen, E. L. Thomas, Defects, solvent quality, and photonic response in lamellar block copolymer gels. *Macromolecules* **47**, 1130–1136 (2014).
28. A. Repular, E. Grelet, Elementary edge and screw dislocations visualized at the lattice periodicity level in the smetic phase of colloidal rods. *Phys. Rev. Lett.* **121**, 097801 (2018).
29. R. L. Blumberg Selinger, Diffusion in a smectic liquid crystal with screw dislocations. *Phys. Rev. E* **65**, 051702 (2002).
30. J. Y. Chung, A. J. Nolte, C. M. Stafford, Diffusion-controlled, self-organized growth of symmetric wrinkling patterns. *Adv. Mater.* **21**, 1358–1362 (2009).
31. S. Chada, M. Yan, Self-assembled nanostructures from homopolymer induced by UV and solvent exposure. *Soft Matter* **4**, 2164–2167 (2008).
32. E. P. Chan, A. J. Crosby, Spontaneous formation of stable aligned wrinkling patterns. *Soft Matter* **2**, 324–328 (2006).
33. Y.-C. Chen, A. J. Crosby, High aspect ratio wrinkles via substrate prestretch. *Adv. Mater.* **26**, 5626–5631 (2014).
34. Y. Ebata, A. B. Croll, A. J. Crosby, Wrinkling and strain localizations in polymer thin films. *Soft Matter* **8**, 9086–9091 (2012).
35. D.-Y. Khang, H. Jiang, Y. Huang, J. A. Rogers, A stretchable form of single-crystal silicon for high-performance electronics on rubber substrates. *Science* **311**, 208–212 (2006).
36. N. C. Bec Tan, D. G. Peiffer, R. M. Briber, Reactive reinforcement of polystyrene/poly (2-vinylpyridine) interfaces. *Macromolecules* **29**, 4969–4975 (1996).
37. Z. Huang, W. Hong, Z. Suo, Evolution of wrinkles in hard films on soft substrates. *Phys. Rev. E* **70**, 03601 (2004).
38. R. Al-Rashed, F. L. Jimenez, J. Marthelot, P. M. Reis, Buckling patterns in biaxially pre-stretched bilayer shells: Wrinkles, creases, folds and fracture-like ridges. *Soft Matter* **13**, 7969–7978 (2017).
39. D. L. Medin, Unraveling the dislocation core structure at a van der Waals gap in bismuth telluride. *Nat. Commun.* **10**, 1820 (2019).
40. A. M. Walker, Predicting the structure of screw dislocations in nanoporous materials. *Nat. Mater.* **3**, 715–720 (2004).
41. M. P. Stoykovich, M. Müller, S. O. Kim, H. H. Solak, E. W. Edwards, J. J. De Pablo, P. F. Nealey, Directed assembly of block copolymer blends into nonregular device-oriented structures. *Science* **308**, 1442–1446 (2005).

42. A. Honglawan, D. A. Beller, M. Cavallaro, R. D. Kamien, K. J. Stebe, S. Yang, Topographically induced hierarchical assembly and geometrical transformation of focal conic domain arrays in smectic liquid crystals. *Proc. Natl. Acad. Sci. U.S.A.* **110**, 34–39 (2013).
43. M. J. Shin, D. K. Yoon, Role of stimuli on liquid crystalline defects: From defect engineering to switchable functional materials. *Materials* **13**, 5466 (2020).
44. S. Park, K. Koo, K. Kim, H. Ahn, B. Lee, C. Park, D. Y. Ryu, Transition behavior of asymmetric polystyrene-b-poly (2-vinylpyridine) films: A stable hexagonally modulated layer structure. *Polymer* **60**, 32–39 (2015).
45. M. Pinna, S. Hiltl, X. Guo, A. Böker, A. V. Zvelindovsky, Block copolymer nanocontainers. *ACS Nano* **4**, 2845–2855 (2010).
46. J. Huh, J. Y. Jung, J. U. Lee, H. Cho, S. Park, C. Park, W. H. Jo, Supramolecular assembly of end-functionalized polymer mixtures confined in nanospheres. *ACS Nano* **5**, 115–122 (2011).
47. T. C. Beutler, A. E. Mark, R. C. van Schaik, P. R. Gerber, W. F. van Gunsteren, Avoiding singularities and numerical instabilities in free energy calculations based on molecular simulations. *Chem. Phys. Lett.* **222**, 529–539 (1994).
48. R. L. C. Akkermans, N. A. Spenley, S. Robertson, COMPASS III: Automated fitting workflows and extension to ionic liquids. *Mol. Simul.* **47**, 540–551 (2021).
49. A. A. Samoletov, C. P. Dettmann, M. A. J. Chaplain, Thermostats for "slow" configurational modes. *J. Stat. Phys.* **128**, 1321–1336 (2007).
50. H. J. C. Berendsen, J. P. M. Postma, W. F. van Gunsteren, A. DiNola, J. R. Haak, Molecular dynamics with coupling to an external bath. *J. Chem. Phys.* **81**, 3684–3690 (1984).

Acknowledgments

Funding: This research was supported by the National Research Foundation of the Korean government (MEST) (grant no. 2020R1A2B5B03002697) and the Creative Materials Discovery Program funded by the Ministry of Science and ICT (grant no. NRF-2018M3D1A1058536). This project also received support from KIST Institutional Program (project no. 2Z05900-19-P096) and the Brain Korea 21 Plus project's four stages. The work at TAMU was supported by the Hagler Institute Fellowship to E.L.T. J.H. acknowledges support from the National Research Foundation of Korea (no. 2020R1A4A2002903). **Author contributions:** Cheolmin Park, J.H., and E.L.T. supervised the research. H.S.K. and Chanho Park conceived the idea and developed the overall characterizations of a screw dislocation with various methods. H.E. and C.E.L. used the AFM to characterize the morphology of screw dislocation in solvent condition. D.Y.R. synthesized the PS-*b*-P2VP BCP. J.H. also mathematically modeled the screw dislocation. Y.K. and X.F. developed the characterization of the screw dislocation from optical microscopy and FIB-SEM. All authors discussed the results and helped write the manuscript. **Competing interests:** The authors declare that they have no competing interests. **Data and materials availability:** All data needed to evaluate the conclusions in the paper are present in the paper and/or the Supplementary Materials.

Submitted 22 September 2021
Accepted 21 January 2022
Published 11 March 2022
10.1126/sciadv.abm5120

ScienceAdvances

Visualization of nonsingular defect enabling rapid control of structural color

Han Sol KangChanho ParkHongkyu EohChang Eun LeeDu Yeol RyuYoungjong KangXuenyan FengJune HuhEdwin L. ThomasCheolmin Park

Sci. Adv., 8 (10), eabm5120. • DOI: 10.1126/sciadv.abm5120

Science Advances (ISSN) is published by the American Association for the Advancement of Science. 1200 New York Avenue NW, Washington, DC 20005. The title *Science Advances* is a registered trademark of AAAS.